

## Seasonal variability of upper ocean heat content in Drake Passage

Gordon R. Stephenson Jr.,<sup>1</sup> Sarah T. Gille,<sup>1,2</sup> and Janet Sprintall<sup>1</sup>

Received 1 December 2011; revised 9 February 2012; accepted 22 February 2012; published 11 April 2012.

[1] Mixed-layer depth (MLD) is often used in a mixed-layer heat budget to relate air-sea exchange to changes in the near-surface ocean temperature. In this study, reanalysis heat flux products and profiles from a 15 year time series of high-resolution, near-repeat expendable bathythermograph/expendable conductivity-temperature-depth (XBT/XCTD) sampling in Drake Passage are used to examine the nature of MLD variations and their impact on a first-order, one-dimensional heat budget for the upper ocean in the regions north and south of the Polar Front. Results show that temperature and density criteria yield different MLD estimates, and that these estimates can be sensitive to the choice of threshold. The difficulty of defining MLD in low-stratification regions, the large amplitude of wintertime MLD (up to 700 m in Drake Passage), and the natural small-scale variability of the upper ocean result in considerable cast-to-cast variability in MLD, with changes of up to 200 m over 10 km horizontal distance. In contrast, the heat content over a fixed-depth interval of the upper ocean shows greater cast-to-cast stability and clearly measures the ocean response to surface heat fluxes. In particular, an annual cycle in upper ocean heat content is in good agreement with the annual cycle in heat flux forcing, which explains  $\sim 24\%$  of the variance in heat content above 400 m depth north of the Polar Front and  $\sim 63\%$  of the variance in heat content south of the Polar Front.

**Citation:** Stephenson, G. R., Jr., S. T. Gille, and J. Sprintall (2012), Seasonal variability of upper ocean heat content in Drake Passage, *J. Geophys. Res.*, 117, C04019, doi:10.1029/2011JC007772.

### 1. Introduction

[2] The Southern Ocean has experienced statistically significant warming over the past few decades [Böning *et al.*, 2008; Gille, 2008; Levitus *et al.*, 2009]. Warming of the interior ocean contributes to thermosteric sea level rise [Church *et al.*, 2011], but heat uptake by the ocean may also act to slow the warming of the atmosphere associated with anthropogenic forcing [Boé *et al.*, 2009]. Intermediate water properties of much of the world ocean are set by air-sea interactions in the Southern Ocean [Hanawa and Talley, 2001]. In recent decades, Subantarctic Mode Water and Antarctic Intermediate Water have shown changes consistent with surface warming and increased precipitation in their Southern Ocean source regions [Bindoff and McDougall, 2000; Durack and Wijffels, 2010]. Understanding the rate at which heat is transferred from the atmosphere through the upper layers of the Southern Ocean will help us better determine the effects of global warming on both the ocean and the atmosphere.

[3] In many studies of air-sea exchange, the limit of the upper ocean is defined to be the mixed layer. The mixed-layer depth (MLD) can be used to relate near-surface

temperature changes to the heat fluxes in and out of the mixed layer [e.g., Kuhnelt and Henderson-Sellers, 1991; Qiu and Kelly, 1993; Dong *et al.*, 2007]. In the Southern Ocean, several mixed-layer depth climatologies have been developed [e.g., Kara *et al.*, 2003; de Boyer Montégut *et al.*, 2004; Dong *et al.*, 2008; Holte and Talley, 2009]. However, the MLD values in these climatologies differ depending on the methods (e.g., threshold difference, gradient, hybrid algorithm) [Holte and Talley, 2009] and parameters (e.g., temperature vs. density) [de Boyer Montégut *et al.*, 2004] that are used to determine MLD. In the Southern Ocean, weak stratification or temperature inversions are common [Dong *et al.*, 2008] and may contribute to the disagreement between estimates of MLD. Differences in Southern Ocean MLD estimates contribute to uncertainty not only in Southern Ocean heat budgets [Dong *et al.*, 2007] but in global climate models as well. For example, MLD differences are a major cause of inter-model spread in the projected rate of heat transfer to the ocean interior and hence to the projected rate of increase of globally averaged surface air temperature in the next 100 years [Boé *et al.*, 2009]. This underscores the importance of determining accurate and reliable estimates of vertical heat transfer in the Southern Ocean.

[4] In fact, the choice to use MLD as the representative length scale for vertical mixing of heat within the upper ocean is not obvious. In their seminal paper, Price *et al.* [1986] introduced a vertical-mixing model (known as “PWP”) that is now widely used to study the temporal evolution of the upper ocean, including the mixed layer. In

<sup>1</sup>Scripps Institution of Oceanography, University of California, San Diego, La Jolla, California, USA.

<sup>2</sup>On sabbatical at Laboratoire d'Etudes en Géophysique et Océanographie Spatiales, Observatoire Midi-Pyrénées, Toulouse, France.

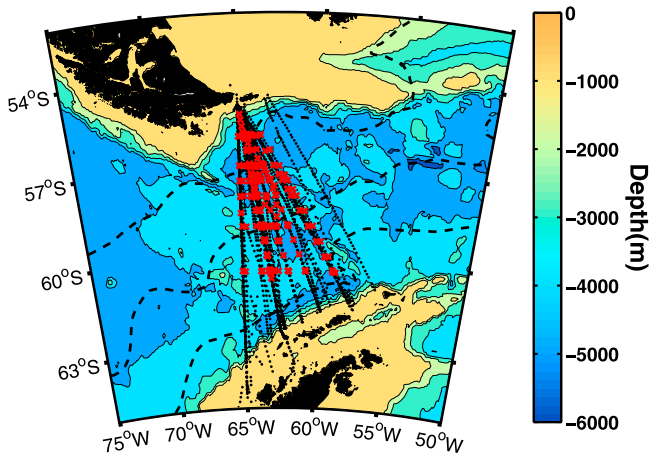


**Figure 1.** Map of Drake Passage showing the locations of the expendable bathythermograph (XBT) (black dots) and expendable conductivity-temperature-depth (XCTD) (red crosses) casts. The climatological mean frontal positions [Orsi *et al.*, 1995] of (from north to south) the Subantarctic Front, Polar Front, and Southern Antarctic Circumpolar Current Front are indicated (dashed lines).

the same study, Price *et al.* [1986] acknowledged some limitations of MLD. Calculating MLD is an attempt to define a quasi-homogeneous layer, where water properties (often temperature or density) are roughly uniform; the degree of desired homogeneity can be tuned by requiring that water properties vary by less than a specified amount. When stratification in the upper ocean is weak, MLD estimates can be sensitive to the specified degree of non-homogeneity. Price *et al.* [1986] addressed this limitation and discussed two other vertical length scales: “trapping depth” is the weighted average depth of the temperature anomaly above a reference depth; “penetration depth” is a depth derived by relating the rate of change of near-surface temperature to changes in the upper ocean heat content. In the following, we will show that upper ocean heat content itself can be a useful measure of ocean uptake of heat from the atmosphere.

[5] Surface forcing is one of the main drivers of upper ocean variability, providing the energy input for seasonal cycles in oceanic heating and cooling. A good measure of upper ocean variability will reflect the changes in ocean state corresponding to such forcing; however, other processes can also influence the upper ocean. Horizontal advection in the form of eddies and frontal meanders, for example, can cause a strong warming or cooling signal through the upper 1000 m of the water column [e.g., Joyce *et al.*, 1981]. Vertical entrainment and mixing within the upper ocean redistribute heat internally and are a source of upper ocean variability. To the extent that these processes are occurring in the upper ocean, the relationship between surface forcing and parameters representing the state of the upper ocean becomes less immediate and more difficult to discern.

[6] This study will compare the characteristics of several measures of upper ocean variability and evaluate their utility as measures of the ocean’s response to surface heating. We focus on the Drake Passage, where a 15 year time series of

profile data from expendable probes along a near-repeat transect allows estimation of the seasonal patterns of surface heat forcing and the oceanic response. Section 2 describes the upper ocean data and the heat flux products used in the analysis. Section 3 compares characteristics of MLD and heat content. Section 4 relates seasonal patterns in surface forcing, mixed-layer heat content and upper ocean heat content. We present a simplified two-term (temperature tendency and total heat flux) seasonal heat budget for the upper ocean and assess its validity in the Drake Passage. Section 5 summarizes our findings.

## 2. Data

### 2.1. XBT and XCTD Profiles

[7] Variability in the upper ocean is examined using data collected as part of the high-resolution expendable bathythermograph (XBT)/expendable conductivity-temperature-depth (XCTD) sampling program [Sprintall, 2003] in Drake Passage (Figure 1). Since 1996, approximately 6–7 XBT transects have been undertaken each year, resulting in a total of 91 transects to February 2010. Each transect typically takes 2–3 days to complete. Approximately 70 XBTs are dropped per transect. XBT casts are spaced 10–15 km apart, except when crossing the Subantarctic Front and the Polar Front, where casts are spaced 6–10 km apart. XBTs return temperature at 2 m vertical resolution to a depth of  $\sim 850$  m. The fall-rate correction of Hanawa *et al.* [1995] has been applied to each profile. Most transects after 2001 also include  $\sim 10$ –12 XCTD profiles, spaced 25–50 km apart (Figure 1). XCTDs return profiles to  $\sim 1100$  m of temperature ( $T$ ) and conductivity, from which salinity ( $S$ ) and density ( $\rho$ ) can be calculated. The effective vertical resolution of the XCTDs is at best about 0.7 m [Gille *et al.*, 2009]. In this analysis, we have smoothed the XCTD  $T$ ,  $S$ , and  $\rho$  to an effective resolution of 2 m using a low-pass filter (11 point least squares, passband = 0.07, stop band = 0.10) and then sub-sampled at 2 m depth increments.

[8] When an XBT or XCTD is deployed, the probe requires a few seconds to equilibrate to the seawater temperature. Hence, the top 10 m of a cast may contain spurious temperatures. For this study, temperature values shallower than 10 m were replaced with the 11 m temperature value; one result of this replacement is that temperature is assumed to be well-mixed to at least 11 m depth.

[9] Of the 91 XBT/XCTD transects, three cruises (September 1999, June 2000, and January 2009) deviated significantly from the typical crossings outlined in Figure 1 and another three (February 1998, May 1998, and July 1999) surveyed only the northern half of Drake Passage, likely due to sea ice or foul weather. Data from these cruises have been omitted from our analysis (accounting for 372 XBT casts and 11 XCTD casts). In addition, while 70% of casts reached 800 m depth, casts that do not reach at least 400 m depth are omitted as they may not fully resolve the mixed layer. From the 85 XBT/XCTD transects we considered for this study, we have included 5071 of a possible 5637 XBT casts and 343 of a possible 360 XCTD casts. Of these, 2668 XBT and 213 XCTD casts were collected north of the Polar Front, defined here as the northward extent of the  $2^{\circ}\text{C}$  isotherm at 200 m depth [Orsi *et al.*, 1995], and

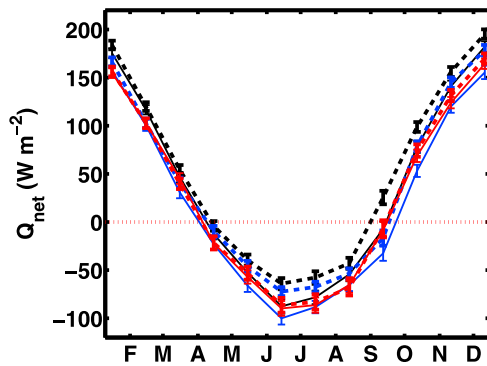


**Figure 2.** Monthly heat flux climatologies for NCEP (red), J-OFURO (blue), and OAFlux (black) over regions north (solid line) and south (dashed line) of the climatological position of the Polar Front. Vertical lines indicate the two-sigma standard error of a 30 day average.

2403 XBT casts and 130 XCTD casts were collected south of the Polar Front.

## 2.2. Heat Fluxes

[10] In situ meteorological observations needed to determine the air-sea exchanges that comprise surface heat fluxes are sparse in the Southern Ocean. Several remote-sensing and reanalysis products provide estimates of the net heat flux into the ocean, but these products may differ by more than their uncertainties [e.g., *Dong et al.*, 2007]. Furthermore, systematic errors in estimates of high-latitude cloud cover cause a positive bias in the reanalysis surface heat fluxes over the Southern Ocean [*Trenberth and Fasullo*, 2010]. As a result, surface heat fluxes are a major source of error in Southern Ocean heat budgets. To allow for the expected differences between heat flux products, we compared the daily, gridded heat fluxes of three products: NCEP-NCAR reanalysis, a  $\sim 1.9^\circ \times 1.9^\circ$  resolution product that we have sampled over 1 January 1996 to 31 December 2010; Japanese Ocean Flux data set with Use of Remote Observations (J-OFURO [*Kubota et al.*, 2002]), at  $1^\circ \times 1^\circ$  resolution from 1 January 1997 to 31 December 2006; and Objectively Analyzed Fluxes (OAFlux [*Yu and Weller*, 2007]), at  $1^\circ \times 1^\circ$  resolution from 1 January 1996 to 31 December 2007. Only the data set from the NCEP-NCAR reanalysis overlapped the full time span of the XBT/XCTD transects (1996–2010); however, both J-OFURO and OAFlux flux

products spanned 10 or more years, which should be sufficient to examine the annual cycle.

[11] For each heat flux product, spatial averages were computed for regions north ( $56\text{--}59^\circ\text{S}$ ,  $60\text{--}64^\circ\text{W}$ ) and south ( $59\text{--}62^\circ\text{S}$ ,  $60\text{--}64^\circ\text{W}$ ) of the climatological position of the Polar Front [*Orsi et al.*, 1995] in Drake Passage. The climatological position of the Polar Front was used rather than the instantaneous position because we are also interested in determining the heat accumulating in the time intervals between transects, when there are no XBT data available to confirm the location of the Polar Front. Since the heat fluxes are fairly smooth [*Dong et al.*, 2007], small shifts in the location of the Polar Front should not affect our results. For each heat flux product and region (north or south of the Polar Front), a monthly climatology of  $Q_{net}$  values was constructed (Figure 2). The maximum heat input into the ocean ( $\sim 150$  to  $200 \text{ W m}^{-2}$ ) occurs in December, while the greatest heat loss from the ocean surface ( $-100$  to  $-50 \text{ W m}^{-2}$ ) occurs in June (Figure 2). The annual cycle in heat fluxes is nearly sinusoidal; to quantify the amplitude and phase of the seasonal cycle, we least squares fit a sinusoid with a period of 365.25 days to the time series of heat fluxes; this fit explained 64% of the variance in NCEP heat fluxes, 73% of the variance in OAFlux, and 74% of the variance in J-OFURO fluxes. Uncertainties were computed by multiplying the error estimates from the least squares fitting procedure by the standard deviation of the heat flux values. A Monte Carlo method with  $N = 10^5$  was used to calculate the uncertainty on the date of maximum amplitude.

[12] The mean annual heat flux is positive (into the ocean) for all of the heat flux products (Table 1), with OAFlux indicating the largest mean net heat flux into the ocean both north and south of the Polar Front. All heat flux products show that the mean net heat flux is greater south of the Polar Front than north (Table 1). This north–south difference is greatest for J-OFURO ( $16 \text{ W m}^{-2}$ ). NCEP fluxes, with lower spatial resolution, showed a cross-frontal difference of only  $2 \text{ W m}^{-2}$ , which was smaller than the uncertainties in the annual mean. Despite the differences in the annual mean values of net air-sea heat flux, the amplitudes ( $\sim 130 \text{ W m}^{-2}$ ) and phases (maximum within a few days of December 25) of the seasonal cycles in surface heating were remarkably similar between all products (Figure 2, Table 1) and for the regions north and south of the Polar Front. In situ observations in Drake Passage have also found no significant differences in the seasonal cycle of turbulent heat fluxes across the Polar Front [*Dong et al.*, 2007; *Jiang et al.*, 2012]. In this

**Table 1.** Annual Mean Net Heat Fluxes Computed From NCEP, J-OFURO, and OAFlux Heat Flux Products, Averaged Over Grid Points North ( $56^\circ\text{--}59^\circ\text{S}$ ) and South ( $59^\circ\text{--}62^\circ\text{S}$ ) of the Climatological Position of the Polar Front in the Longitude Range  $60^\circ\text{--}64^\circ\text{W}^a$

Heat Flux Product	Region	Annual Mean $Q_{net}$ ( $\text{W m}^{-2}$ )	Amplitude of Cycle ( $\text{W m}^{-2}$ )	Date of Maximum Amplitude
NCEP	north of PF	$29.5 \pm 1.6$	$130 \pm 3.2$	25 Dec $\pm 1$ day
	south of PF	$31.7 \pm 1.6$	$131 \pm 3.2$	24 Dec $\pm 1$ day
J-OFURO	north of PF	$22.1 \pm 1.8$	$131 \pm 3.6$	27 Dec $\pm 1$ day
	south of PF	$41.6 \pm 1.9$	$127 \pm 3.7$	25 Dec $\pm 1$ day
OAFlux	north of PF	$39.4 \pm 1.7$	$137 \pm 3.4$	25 Dec $\pm 1$ day
	south of PF	$56.3 \pm 1.9$	$131 \pm 3.8$	22 Dec $\pm 1$ day

<sup>a</sup>A least squares fit to a sinusoid with period 365.25 days gives the amplitude and phase of the annual cycle. One-sigma uncertainties were computed by multiplying the error estimates from the least squares fitting procedure by the standard deviation of the heat flux values. A Monte Carlo method with  $N = 10^5$  was used to calculate the uncertainty on the date of maximum amplitude.

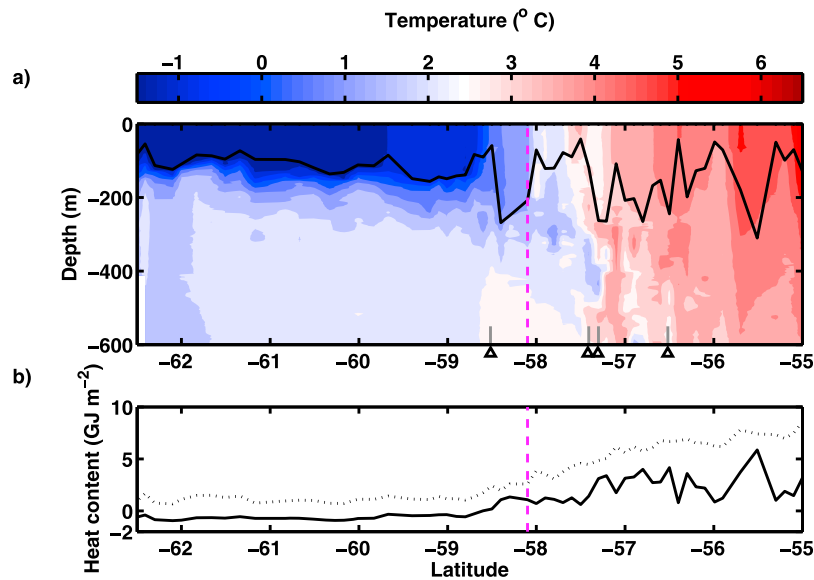


**Figure 3.** (a) A section of temperature ( $^{\circ}\text{C}$ ) from XBT casts during a Drake Passage transect 18–23 September 2009. The position of the Polar Front is indicated by the dashed magenta line. Mixed-layer depth (MLD) is indicated by the black line. The latitude of example casts in Figures 4 and 5 are also indicated (triangles). (b) Mixed-layer heat content (solid black) and heat content integrated to 400 m (dashed line) for XBT casts from the transect in Figure 3a.

study, we examine the seasonal cycle in heat flux after the annual mean (Table 1) has been removed. After removing an annual mean, we found little difference between heat flux products or between regions north and south of the Polar Front; therefore, in the following we will use only the results from NCEP heat fluxes north of the Polar Front to represent the annual cycle in heat flux forcing in Drake Passage.

### 3. Measures of Upper Ocean Variability

[13] In Drake Passage, the Polar Front represents a boundary between two regions with distinct water mass characteristics. The difference is clearly visible in a section of temperature across Drake Passage, collected in late September 2009 at the end of austral winter (Figure 3a). South of the Polar Front, Antarctic Surface Water (AASW) of the upper layer is colder than the upper Circumpolar Deep Water immediately below it. In summer, this cold layer is capped by warmer water, but a temperature minimum (inversion) at  $\sim 150$  m is nearly always present. The temperature inversion is density-compensated by salinity that increases with depth [Sprintall, 2003].

[14] North of the Polar Front, temperature stratification is weak and temperature generally decreases as depth increases, although occasionally small-amplitude inversions related to water mass interleaving and eddy mixing occur at depth [e.g., Sprintall, 2003]. The differences in water column structure north and south of the Polar Front complicate efforts to understand the upper ocean variability of both regions using MLD. This section explores the robustness and the small-scale spatial variability of MLD as compared to the use of upper ocean heat content.

[15] Two other parameters that measure upper ocean variability, trapping depth ( $D_T$ ) and penetration depth ( $D_p$ ),

were also explored.  $D_T$  is essentially the mean depth of the temperature anomaly in the upper ocean [Price *et al.*, 1986],

$$D_T = \frac{1}{T(z_{ref}) - T(0)} \int_{-z_{ref}}^0 z(T(z) - T(0))dz, \quad (1)$$

where  $T$  is temperature and  $z_{ref}$  is a lower reference depth. South of the Polar Front, the permanent temperature inversion makes the denominator in (1) close to zero or negative for  $z_{ref} \geq 200$  m, leading to spurious values for  $D_T$ . Hence  $D_T$  does not provide a useful measure of upper ocean variability in Drake Passage.  $D_p$  infers the depth to which heat fluxes are mixed by tracking changes in sea surface temperature (SST) and upper ocean heat content. This requires a time series with more regular sampling than is available from our XBT time series in Drake Passage, so  $D_p$  is also not suited to the purposes of this study.

#### 3.1. Mixed-Layer Depth

[16] Two methods are typically employed to identify mixed-layer depth. The threshold (also known as finite difference) method defines MLD as the depth at which a water property differs by a fixed amount from its surface value. In contrast, gradient methods determine MLD by locating a strong vertical gradient in a water property. The two methods often give different MLDs even in an idealized upper ocean density profile, as they rely on choices of predetermined threshold and gradient [e.g., Holte and Talley, 2009]. In the real ocean, the threshold method is more stable than the gradient method because profiles of the vertical derivatives of temperature or salinity are generally noisier than the properties themselves [Brainerd and Gregg, 1995]. Holte and Talley [2009] developed a hybrid approach that applies several techniques, including threshold and gradient

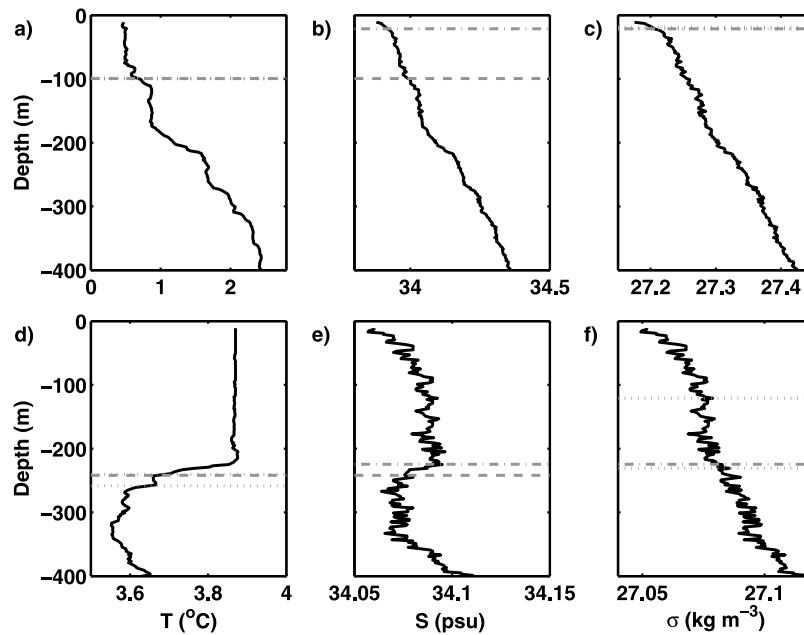


**Figure 4.** Profiles from XCTD casts collected during the transect shown in Figure 3 on (a–c) 20 September 2009 near 58.5°S, 63.7°W and on (d–f) 19 September 2009 near 56.5°S, 64.1°W. Profiles show temperature (°C, Figures 4a and 4d), salinity (psu, Figures 4b and 4e), and potential density ( $\text{kg m}^{-3}$ , Figures 4c and 4f).  $\text{MLD}_T$  is shown by the dashed line (Figures 4a, 4b, 4d, 4e), and  $\text{MLD}_\rho$  is shown by the dash-dotted lines (Figures 4b, 4c, 4e, 4f). Dotted lines show differences in  $\text{MLD}_T$  (Figures 4a and 4d) and  $\text{MLD}_\rho$  (Figures 4c and 4f) after  $\Delta T$  and  $\Delta\rho$  are changed by  $\pm 10\%$ , respectively. In Figures 4a and 4c, these lines lie very close to the dashed line indicating  $\text{MLD}_T$ . Note also that the x-axis scale is different for the top and bottom plots.

methods, to identify candidate MLDs and then selects one based on physical characteristics of the profile. To simplify comparison with mixed-layer climatologies, in this study we present results using the threshold method. The simplicity of the threshold difference also enables us to identify the cause of variations in MLD estimates between different profiles. Qualitatively similar results are obtained if MLD is calculated with the gradient method or the algorithm of *Holte and Talley* [2009].

[17] We consider two variants of the threshold method of determining MLD. The first,  $\text{MLD}_T$ , is computed using a temperature threshold and is defined so that the base of the mixed layer at  $z_{ML}$  is the shallowest depth such that  $|T(z_{ML}) - T_0| \geq \Delta T$ , where  $T_0$  is the near-surface temperature (at 11 m), and  $\Delta T$  is the difference threshold. The presence of temperature inversions (Figure 3a) makes the absolute value in this definition necessary. The second,  $\text{MLD}_\rho$ , is computed using a density threshold, finding  $z_{ML}$  such that  $|\rho(z_{ML}) - \rho_{sfc}| \geq \Delta\rho$ . While *Holte and Talley* [2009] found that MLD estimates based on density are generally more accurate than those based only on temperature, the abundance of temperature profiles and relative lack of density profiles make consideration of both types of MLD estimates necessary. Following other studies of MLD in the Southern Ocean [e.g., *de Boyer Montégut et al.*, 2004; *Dong et al.*, 2008], we use a temperature threshold ( $\Delta T$ ) of  $0.2^\circ\text{C}$  and a potential density threshold ( $\Delta\rho$ ) of  $0.03 \text{ kg m}^{-3}$ .

[18] Differences in  $\text{MLD}_T$  and  $\text{MLD}_\rho$  can occur where significant salinity changes occur with depth. A wintertime

profile south of the Polar Front (at 58.5°S, 63.7°W) (Figures 4a–4c) shows temperature and salinity both increase with depth, but a salinity gradient near the surface is not mirrored in the temperature profile. As a result  $\text{MLD}_\rho$  is 80 m shallower than  $\text{MLD}_T$ . By contrast, in a wintertime profile north of the Polar Front (at 56.5°, 64.1°W) (Figures 4d–4f), the salinity gradient is much weaker, and  $\text{MLD}_\rho$  is only 18 m shallower than  $\text{MLD}_T$ .

[19] Seasonal and regional differences between  $\text{MLD}_T$  and  $\text{MLD}_\rho$  are reflected in the cumulative distribution functions of  $\text{MLD}_T - \text{MLD}_\rho$  (Figure 5a).  $\text{MLD}_T$  is typically deeper than  $\text{MLD}_\rho$  (i.e., right of 0-line in Figure 5a). In our Drake Passage data set, we find that  $\text{MLD}_T$  is greater than  $\text{MLD}_\rho$  by at least 10 m in 58% of all casts, while in 38% of casts,  $\text{MLD}_T$  and  $\text{MLD}_\rho$  differ by less than 10 m. The difference between  $\text{MLD}_T$  and  $\text{MLD}_\rho$  is generally smaller in summer (December to March) than winter (June to September) (Figure 5a; Table 2) and is smaller on average south of the Polar Front than north (Table 2). In 4% of casts,  $\text{MLD}_T$  is shallower than  $\text{MLD}_\rho$  by more than 10 m. These casts are characterized by density-compensating layers, occur mostly in winter, and are more often found south of the Polar Front than north.

[20] The difference between  $\text{MLD}_T$  and  $\text{MLD}_\rho$  varies with the upper ocean temperature stratification, which, in turn, varies seasonally and by region. Our results agree with those of *Holte and Talley* [2009], who found that  $\text{MLD}_T$  tends to overestimate the depths of deep mixed layers relative to  $\text{MLD}_\rho$ , and suggest that temperature is not always adequate for accurately determining MLD. This is especially the case

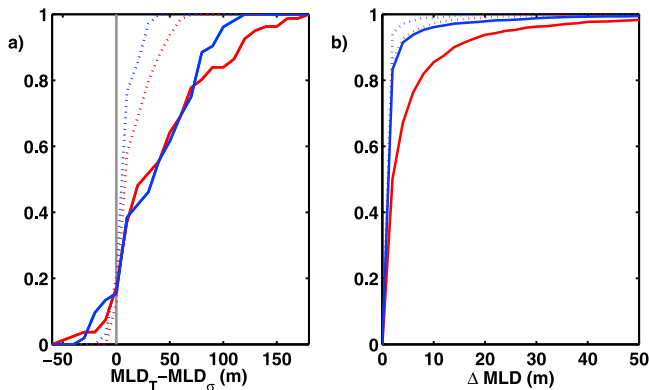


**Figure 5.** (a) Cumulative distribution functions (CDFs) of the difference between  $MLD_T$  and  $MLD_\rho$  (i.e.,  $MLD_T - MLD_\rho$ ) and (b) CDFs of the change in  $MLD_T$  in response to a  $\pm 10\%$  perturbation to  $\Delta T$  for XCTD casts collected in winter (solid line) and summer (dotted line), north (red) or south (blue) of the Polar Front.

in winter, when Drake Passage is characterized by deep mixing and low stratification. In the absence of strong vertical density or temperature gradients, it can be difficult to unambiguously determine the true depth of mixing using MLD. To test the robustness of MLD estimates to the choice of threshold, we perturbed  $\Delta T$  by  $\pm 0.02^\circ\text{C}$  and  $\Delta\rho$  by  $\pm 0.003\text{ kg m}^{-3}$ , a  $\pm 10\%$  change to the threshold criteria used to compute  $MLD_T$  and  $MLD_\rho$ , respectively. This procedure is equivalent to perturbing the near-surface temperature or density by the same amount, making this test also a measure of how much MLD might change in response to a small surface heat or buoyancy exchange.

[21] An example of the 10% perturbation in threshold is shown for a typical winter profile from an XCTD cast north of the Polar Front (at  $56.5^\circ\text{S}$ ,  $64.1^\circ\text{W}$ ) (Figures 4d–4f).  $MLD_T$  has been computed using the original threshold criteria of  $\Delta T = 0.20^\circ\text{C}$  (dashed line in Figure 4d), and the 10% perturbations  $\Delta T = 0.18^\circ\text{C}$  (top dotted line in Figure 4d) and  $\Delta T = 0.22^\circ\text{C}$  (lower dotted line in Figure 4d). Decreasing the temperature threshold  $\Delta T$  reduces  $MLD_T$  from 242 m to 240 m, while increasing  $\Delta T$  deepens  $MLD_T$  to 258 m (Figure 4d).  $MLD_\rho$  is much more sensitive to the change in  $\Delta\rho$  threshold; reducing  $\Delta\rho$  from 0.030 to  $0.027\text{ kg m}^{-3}$  decreased  $MLD_\rho$  from 220 m to 120 m (Figure 4f), while increasing  $\Delta\rho$  increased  $MLD_\rho$  to 230 m. By contrast, for the cast collected south of the Polar Front (at  $58.5^\circ\text{S}$ ,

$63.7^\circ\text{W}$ ) a 10% perturbation to  $\Delta T$  and  $\Delta\rho$  changed  $MLD_T$  and  $MLD_\rho$  by less than 2 m (Figures 4a–4c).

[22] The average  $MLD_T$  change in response to a threshold perturbation is larger north of the Polar Front than south and is larger in winter than summer (Table 2). A cumulative distribution function of changes in  $MLD_T$  shows that perturbing the threshold results in a small (5 m or less) change in  $MLD_T \sim 85\%$  of the time, except during winter (June–September) north of the Polar Front (Figure 5b). The reduced sensitivity south of the Polar Front may be a result of the stronger permanent thermocline that provides a lower bound on MLD and results in smaller maximum  $\Delta MLD_T$ . Stronger near-surface temperature gradients in summer account for the reduced summertime sensitivity to threshold. On average,  $MLD_\rho$  and  $MLD_T$  are equally sensitive to threshold perturbations north of the Polar Front, and  $MLD_\rho$  is a little more sensitive than  $MLD_T$  south of the Polar Front (Table 2).

[23] Because MLD is sensitive to small-amplitude noise, small differences between two adjacent profiles may result in large differences in MLD. Two temperature profiles from XBTs deployed only 10 km ( $\sim 1$  h) apart north of the Polar Front (at  $57.3^\circ\text{S}$  and  $57.4^\circ\text{S}$ ,  $64.0^\circ\text{W}$  on 19 September 2009) have  $MLD_T$  of 263 m (Figure 6a) and 118 m (Figure 6b). While these profiles share many features, such as alternating warm and cold layers, a slight warming at 120 m is observed in the southernmost profile (Figure 6b), resulting in MLDs that differ by  $>100$  m.

[24] To quantify the cast-to-cast variability of MLD as observed in Figure 6, we computed the root-mean square (RMS) change in  $MLD_T$  from one cast to the next. We selected 5010 pairs of casts that occurred less than 1 h apart (typically  $<10$  km spacing). The cast-to-cast difference in  $MLD_T$  ( $\pm$  one standard error) is much greater in winter ( $54 \pm 3$  m) than summer ( $20 \pm 1$  m) and is greater north ( $40 \pm 1$  m) than south ( $24 \pm 1$  m) of the Polar Front. This agrees with the examples shown in Figures 3a and 6; south of the Polar Front, MLD variations are small, whereas large MLD changes over short spatial scales are common north of the Polar Front.

### 3.2. Upper Ocean Heat Content

[25] We expect heat content to show a more direct relationship to heat flux forcing than MLD and to be less affected by cross-frontal differences in temperature stratification than MLD. Potentially, this makes heat content a more consistent, more robust, and less noisy measure of upper ocean variability. In this section, we examine whether

**Table 2.** Characteristics of MLD and Heat Content Described by Region (North or South of the Polar Front) and Season (Winter or Summer)<sup>a</sup>

Region	Season	$MLD_T - MLD_\rho$	$\Delta MLD_T$	$\Delta MLD_\rho$	RMS Cast-to-Cast $\Delta\mathcal{H}_{ML}$ ( $\text{GJ m}^{-2}$ )( $N$ )	RMS Cast-to-Cast $\Delta\mathcal{H}_{400}$ ( $\text{GJ m}^{-2}$ )( $N$ )
North of PF	summer	$13 \pm 2$ m	$2.4 \pm 0.6$ m	$3.0 \pm 1.1$ m	0.56 (609)	0.12 (609)
	winter	$48 \pm 7$ m	$7.1 \pm 1.5$ m	$8.2 \pm 2.2$ m	1.99 (429)	0.16 (429)
South of PF	summer	$6 \pm 2$ m	$1.8 \pm 0.4$ m	$2.4 \pm 0.6$ m	0.36 (643)	0.12 (643)
	winter	$34 \pm 5$ m	$4.0 \pm 0.8$ m	$5.2 \pm 1.3$ m	0.95 (560)	0.20 (560)

<sup>a</sup>The average difference in MLD defined using temperature and density criteria ( $MLD_T - MLD_\rho$ ) was computed from XCTD casts.  $\Delta MLD_T$  and  $\Delta MLD_\rho$  are the average changes in calculated MLD in response to a 10% change in the thresholds used to calculate MLD with temperature ( $MLD_T$ ) and density ( $MLD_\rho$ ), respectively. The uncertainties represent one standard error. Cast-to-cast  $\Delta\mathcal{H}_{ML}$  and  $\Delta\mathcal{H}_{400}$  are the RMS differences in mixed-layer heat content and heat content over 400 m depth respectively, over pairs of casts collected less than 1 h (about 10 km) apart.  $N$  is the number of cast-pairs used to compute  $\Delta\mathcal{H}_{ML}$  and  $\Delta\mathcal{H}_{400}$ .

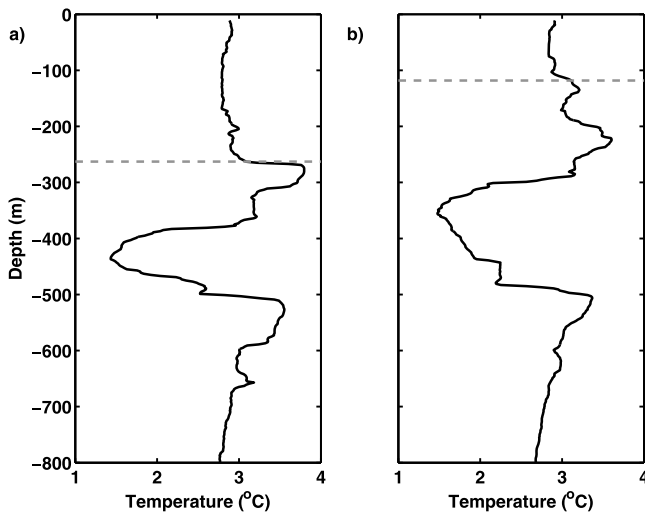


**Figure 6.** Temperature ( $^{\circ}\text{C}$ ) profiles with depth (m) taken 10 km and less than 1 h apart at (a)  $57.4^{\circ}\text{S}$  and (b)  $57.3^{\circ}\text{S}$  near  $64.0^{\circ}\text{W}$ , 19 September 2009, during the transect illustrated in Figure 2. Mixed-layer depths ( $\text{MLD}_T$ , gray dashed line) of 263 m (Figure 6a) and 118 m (Figure 6b) were determined using a  $0.2^{\circ}\text{C}$  temperature threshold.

upper ocean heat content estimated from the Drake Passage data set fulfills this expectation.

[26] We define  $\mathcal{H}_{z_0}$ , the upper ocean heat content integrated from the surface to a depth  $z_0$ , to be

$$\mathcal{H}_{z_0} = \int_{-z_0}^0 \rho_0 c_p T(z) dz, \quad (2)$$

where  $\rho_0 = 1030 \text{ kg m}^{-3}$  is a reference density,  $c_p = 3895 \text{ J kg}^{-1}\text{C}^{-1}$  is the specific heat capacity of seawater,  $T(z)$  is the depth-varying temperature, and  $z_0$  is an integration depth to be determined so as to capture the full effect of surface forcing. To assess an appropriate integration depth, the heat content within 50 m layers between 0 and 800 m depth was computed. Figure 7a shows the standard deviation of the heat content over each depth interval for all casts, binned north and south of the Polar Front. South of the Polar Front, the amplitude of variations is small below about 200 m depth, while north of the Polar Front heat content variability has more significant amplitude down to  $\sim 600$  m.

[27] Figure 7b shows the correlation of heat content in the surface layer (0–50 m) with heat content deeper in the water column. South of the Polar Front, this correlation appears similar to the standard deviation (Figure 7a); surface heat content changes are significantly correlated with heat content changes in layers above 200 m. North of the Polar Front, significant correlation with surface layer heat content are found in layers above  $\sim 350$  m. Changes below this depth are uncorrelated with heat content changes in the surface layer (Figure 7b), but still represent a significant fraction of the variability present north of the Polar Front (Figure 7a). The vertical coherence of this additional heat content variability below 350 m is shown by the correlation of heat content in the layer at 750–800 m, the deepest layer for which we had reliable XBT profiles, with heat content in the rest of the water column (Figure 7b). Heat content changes at

750–800 m are well-correlated ( $r > 0.8$ ) with heat content changes in layers below  $\sim 300$  m depth south of the Polar Front and below  $\sim 200$  m depth north of the Polar Front. This level of vertical coherence is typical of the low-stratification environment of the Southern Ocean and is often associated with advective processes [Sokolov and Rintoul, 2009].

[28] This study aims to test the adequacy of a 1-D heat budget in Drake Passage, forced only by surface heat fluxes; other processes, such as advection, may degrade the validity of this first-order heat balance. The choice of integration depth,  $z_0$  in equation (2), reflects a trade-off between capturing as much of the surface-forced signal as possible while avoiding variability unrelated to surface heat fluxes. Based on Figure 7b, a choice of  $z_0 = 400$  m is likely to reflect all of the heat content signal that is significantly correlated with the surface layer; 400 m is deeper than 99% of the  $\text{MLD}_T$  estimates. As noted above, vertically coherent and presumably advective processes below 200 m depth contribute significantly to heat content variability north of the Polar Front. Selecting  $z_0 = 400$  m rather than a deeper integration depth reduces the weight of this variability relative to surface-forced variability, but does not exclude variability resulting from other processes. For  $z_0 = 400$  m, 77% of the vertically integrated temporal and spatial variance in heat content is captured north of the Polar Front and 92% is captured south of the Polar Front. The sensitivity of our results to this choice of  $z_0$  is discussed in section 4.

[29] As noted in the introduction, a number of previous studies have examined the heat budget within the mixed layer [e.g., Qiu and Kelly, 1993; Dong et al., 2007]. To directly compare the variability of heat content in equation (2) with  $\text{MLD}$ , we also examine the heat content within the mixed layer. Mixed-layer heat content,  $\mathcal{H}_{ML}$ , is defined as

$$\mathcal{H}_{ML} = \rho_0 c_p T_{ML} h_{ML}, \quad (3)$$

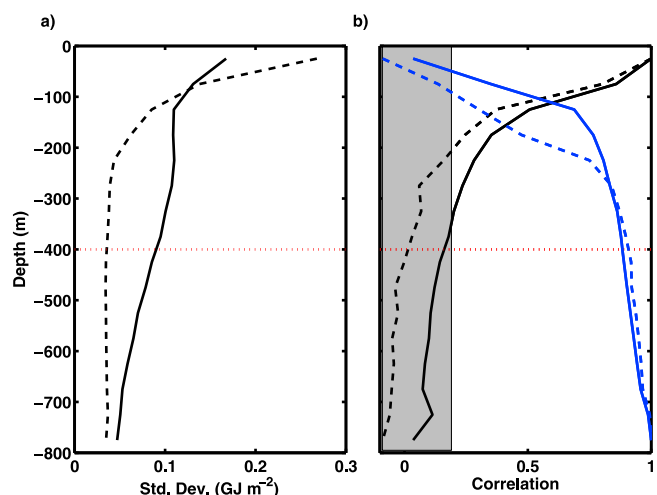


**Figure 7.** (a) Standard deviation of heat content in 50 m layers north (solid) and south (dashed) of the Polar Front. (b) The correlation of heat content in the shallowest layer (0–50 m, black) and in the deepest layer (750–800 m, blue) with heat content in other layers north (solid) and south (dashed) of the Polar Front. The gray bar indicates correlations that are not significant, and the red dotted line delineates 400 m depth.

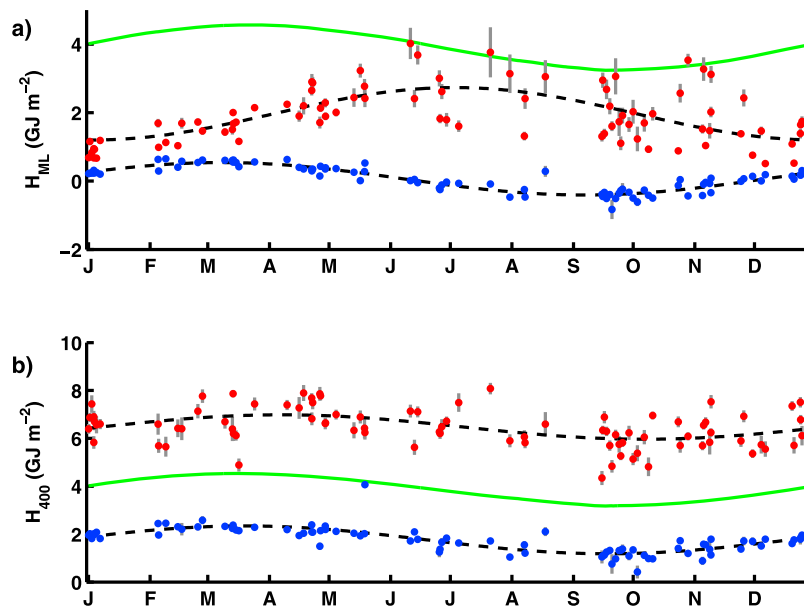


**Figure 8.** (a)  $\overline{\mathcal{H}}_{ML}$ , mean heat content over the mixed layer and (b)  $\overline{\mathcal{H}}_{400}$ , heat content in the upper 400 m of the water column for casts north (red) and south (blue) of the Polar Front for 85 XBT transects are plotted against the median year-day of the cruise. Error bars (gray) represent the standard error of the mean. A sinusoidal annual cycle (dashed lines) is least squares fit to each time series. Surface heat fluxes drive an annual cycle in heat content (green line, offset by  $4 \text{ GJ m}^{-2}$ ) made by integrating daily net heat flux anomalies (annual mean removed) from NCEP.

where  $h_{ML}$  is the depth of the mixed layer ( $MLD_T$ ), and  $T_{ML}$  is the mixed-layer temperature. This quantity is not always directly computed in mixed-layer heat budgets, which more often use  $MLD$  to relate heat fluxes to the rate of change of the mixed-layer temperature, but it provides a good analog for  $\mathcal{H}_{z_0}$  because the units are the same. Mixed-layer heat budgets often assume that the mixed layer is isothermal, and equation (3) represents the mixed-layer heat content under this assumption.

[30] For the XBT/XCTD transect shown in Figure 3a, both  $\mathcal{H}_{400}$  and  $\mathcal{H}_{ML}$  increase with water temperature north of the Polar Front (Figure 3b). Small-scale variability is more pronounced in  $\mathcal{H}_{ML}$ , as it reflects the large changes in  $MLD$  from one cast to the next (e.g., Figure 6), particularly north of the Polar Front. Large fluctuations in  $\mathcal{H}_{400}$  are not as prominent at these small scales. For example, the RMS cast-to-cast difference in  $\mathcal{H}_{ML}$  for the two casts shown in Figure 6 is  $1.7 \text{ GJ m}^{-2}$ , compared with a  $\mathcal{H}_{400}$  difference of only  $0.2 \text{ GJ m}^{-2}$ . This tendency for  $\mathcal{H}_{400}$  to exhibit smaller cast-to-cast variations than  $\mathcal{H}_{ML}$  is true in general. Differences in  $\mathcal{H}_{400}$  and  $\mathcal{H}_{ML}$  cast-to-cast variability are greatest in winter north of the Polar Front: the RMS cast-to-cast  $\Delta\mathcal{H}_{400}$  (separated by  $\sim 10 \text{ km}$ ) is  $<10\%$  of the RMS cast-to-cast  $\Delta\mathcal{H}_{ML}$ , while in summer, the RMS of  $\Delta\mathcal{H}_{400}$  is about 20% as large as the RMS of  $\Delta\mathcal{H}_{ML}$  (Table 2). South of the Polar Front, the differences in cast-to-cast RMS variability are not as extreme; in winter the RMS of  $\Delta\mathcal{H}_{400}$  is about 20% as large as  $\Delta\mathcal{H}_{ML}$ , while in summer the RMS  $\Delta\mathcal{H}_{400}$  is 30% as large as RMS  $\Delta\mathcal{H}_{ML}$  (Table 2). Not only does  $\mathcal{H}_{400}$  exhibit smaller RMS cast-to-cast variability than  $\mathcal{H}_{ML}$ , but it is also more consistent from season to season. Cast-to-cast variability in  $\mathcal{H}_{ML}$  is 3–4 times greater in winter than in summer; for  $\mathcal{H}_{400}$ , RMS cast-to-cast variability in winter is less

than twice as great as in summer (Table 2). This demonstrates one way in which the use of  $MLD_T$  may present a distorted picture of seasonal variability that enhances the apparent upper ocean variability in winter relative to summer. Use of  $\mathcal{H}_{400}$ , with its smaller season-to-season differences in RMS cast-to-cast variability, may reduce this distortion.

#### 4. Seasonal Heating and Cooling of the Upper Ocean

[31] As a first step toward understanding the seasonal variability of upper ocean heat content, we examined the annual pattern of heat fluxes and the expected changes in heat content. As shown in Table 1, the amplitude of the seasonal cycle in heat fluxes is approximately  $130 \text{ W m}^{-2}$ , with a maximum around 25 December. If a heat flux forcing with this amplitude and phase is integrated in time, it yields an annual cycle in heat content of  $\sim 0.66 \text{ GJ m}^{-2}$  that peaks on 25 March (green line, Figures 8a and 8b). In this section, we test whether the mixed-layer and upper ocean heat budgets reflect this seasonal surface heat input.

[32] For our heat budget, we use a simplified first-order relationship between the heat content  $\mathcal{H}$  and the surface forcing  $Q_{net}$  in which

$$\frac{\partial \mathcal{H}}{\partial t} = Q_{net}. \quad (4)$$

This relationship neglects the effects of advection and vertical entrainment on upper ocean heat content. Although these other factors may be important to mixed-layer heat budgets [e.g., Qiu and Kelly, 1993; Dong et al., 2007], our

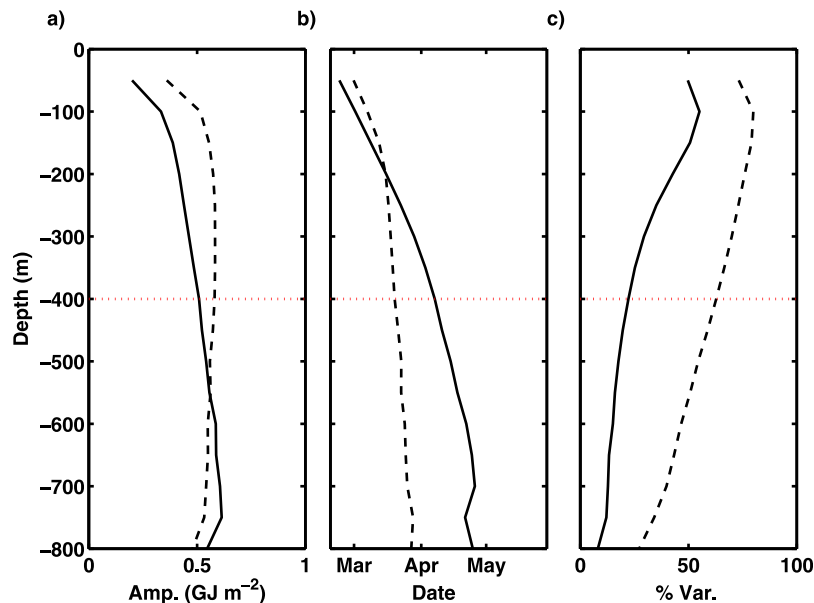


**Figure 9.** (a) Amplitude and (b) phase of a sinusoidal annual cycle fit to  $\overline{\mathcal{H}_{z_0}}$  north (solid) and south (dashed) of the Polar Front for values of  $z_0$  ranging from 50 to 800 m in 50 m increments. (c) The fraction of the variance in  $\overline{\mathcal{H}_{z_0}}$  explained by an annual cycle in heat fluxes. The red dotted line indicates 400 m depth.

main focus here is to isolate the influence of air-sea heat exchange on the ocean to examine the expected first-order terms in the Southern Ocean.

[33] In our estimate of the seasonal cycle in upper ocean heat content, we averaged casts that were collected north of the Polar Front separately from those south of the Polar Front for each of the 85 transects (averages denoted by  $\overline{\mathcal{H}}$ ). The date of each cruise average was assigned as the median date of the casts from each transect. A least squares fit to an annual cycle was made for the time series of  $\overline{\mathcal{H}_{ML}}$  (Figure 8a) and  $\overline{\mathcal{H}_{400}}$  (Figure 8b). North of the Polar Front, a seasonal cycle in  $\overline{\mathcal{H}_{ML}}$  accounts for 38% of the variance and has an amplitude of  $0.77 \text{ GJ m}^{-2}$  with a maximum occurring July 4, in the middle of austral winter (Figure 8a). South of the Polar Front, a seasonal cycle in  $\overline{\mathcal{H}_{ML}}$  with amplitude  $0.47 \text{ GJ m}^{-2}$  peaks on March 7 and explains 83% of the variance in heat content. For  $\overline{\mathcal{H}_{400}}$  north of the Polar Front, an annual cycle with amplitude  $0.51 \text{ GJ m}^{-2}$  peaks on April 8 and explains 24% of the variance (Figure 8b). South of the Polar Front, the annual cycle has an amplitude of  $0.58 \text{ GJ m}^{-2}$ , peaks on March 19, and explains 63% of the variance. There are a number of reasons why the seasonal cycle explains a larger fraction of the variance in  $\overline{\mathcal{H}_{ML}}$  than in  $\overline{\mathcal{H}_{400}}$ . South of the Polar Front, MLD is generally much less than 400 m, so that  $\overline{\mathcal{H}_{ML}}$  reflects variability nearer the surface, where the seasonal pattern of heating and cooling is stronger. North of the Polar Front, a large seasonal change in MLD, from very shallow in summer to very deep in winter, contributes to the stronger seasonality in  $\overline{\mathcal{H}_{ML}}$ . In terms of phase, the deep winter MLDs result in a midwinter (August, Figure 8a) maximum in  $\overline{\mathcal{H}_{ML}}$  that occurs about 4 months after the date at which the cumulative heat input has reached its maximum (March). Thus the phase of the seasonal surface heat input

agrees with the phase of  $\overline{\mathcal{H}_{400}}$  better than with the phase of  $\overline{\mathcal{H}_{ML}}$  (Figure 8a).

[34] We tested whether surface heat input and  $\overline{\mathcal{H}_{z_0}}$  agreed similarly well for other values of the integration depth  $z_0$ . A least squares fit to a sinusoidal annual cycle was made for  $\overline{\mathcal{H}_{z_0}}$  with  $z_0$  ranging from 50 to 800 m varying in 50 m increments. South of the Polar Front, the amplitude of the seasonal cycle changes only slightly with depth below  $\sim 100$  m (Figure 9a). As  $z_0$  increases, the date of the maximum heat content south of the Polar Front is slightly delayed: at  $z_0 = 50$  m the cycle peaks in early March, whereas at  $z_0 = 800$  m the peak occurs in late March (Figure 9b). South of the Polar Front, the heat fluxes explain 80% of the variance at  $z_0 = 100$ , decreasing to 27% at  $z_0 = 800$  m (Figure 9c). North of the Polar Front, the amplitude of the seasonal cycle in heat content changes more with increasing  $z_0$ , from  $0.33 \text{ GJ m}^{-2}$  at  $z_0 = 100$  m to  $0.62 \text{ GJ m}^{-2}$  at  $z_0 = 750$  m (Figure 9a). The peak heat content at  $z_0 = 800$  m occurs in late April, almost 8 weeks later than for  $z_0 = 100$  m in late February (Figure 9b). Heat fluxes explain 55% of the variance in  $\overline{\mathcal{H}_{z_0}}$  at  $z_0 = 100$  m, while less than 25% of the variance is explained for  $z_0 > 400$  m (Figure 9c). At all depths, the amplitude of the annual cycle in heat content was smaller than the  $0.66 \text{ GJ m}^{-2}$  annual cycle in heat input from surface fluxes. *Trenberth and Fasullo* [2010] note that reanalysis heat fluxes over the Southern Ocean have a seasonally varying bias that is greater in summer than winter. Removing such a bias would reduce the amplitude of the annual cycle in heat flux input and may lead to better agreement between the annual cycles in heat content and heat input by surface fluxes.

[35] These results are consistent with the patterns of temperature variance (Figure 7a) that show temperature variations to have higher amplitudes north of the Polar Front than

south, illustrating the differences in vertical heat transfer in the two regions. South of the Polar Front, most heat content fluctuations occur above 200 m (Figure 7a); integrating deeper than 200 m adds very little new information and so changes the seasonal cycle in heat content only slightly. North of the Polar Front, however, a clear depth limit to heat content fluctuations is less evident. Heat concentrates in the upper 100 m during the spring restratification, but this heat is gradually mixed downward. The downward mixing of heat away from the surface results in heating at depth that is delayed relative to the surface (Figure 9b). The maximum temperatures at 650–700 m north of the Polar Front, for example, occur in late May (not shown); however, because we have integrated over the whole water column above this depth, the average date of the maximum in  $\overline{\mathcal{H}}_{700}$  north of the Polar Front occurs in April. Wintertime cooling at the surface results in a nearly isothermal, cool, water column in the upper 800 m north of the Polar Front around September, following which warming and restratification begin anew. The combination of the abrupt cooling in September and the delay in heat transfer from the surface to depth is part of the reason the sinusoidal fit to the integrated heat fluxes in Figure 8 explains less variance as  $z_0$  increases (Figure 9c). The amplitude of the seasonal cycle in surface heating also decreases with depth. This suggests that the 1-D balance between heat fluxes and heat content degrades as  $z_0$  increases, and the relative importance of other processes, such as horizontal heat advection, may come into play. Finally, these results may also have implications for the choice of the integration depth  $z_0$  such that  $\mathcal{H}_{z_0}$  reflects the surface forcing. South of the Polar Front, a choice of  $z_0 > 200$  m appears to provide a sufficient constraint. However, north of the Polar Front the relative importance of surface heating to other processes in determining  $\mathcal{H}_{z_0}$  varies more greatly with depth and suggests greater sensitivity in this region to the choice of  $z_0$ .

[36] The delay of heating with depth in the phase of the seasonal cycle can be used to estimate an effective mixing rate in the upper ocean. In more vigorous mixing regions, surface heating is transported downward more quickly, and so less phase change with depth is observed. Conversely, where mixing is less active, surface heating takes longer to propagate downward, resulting in a longer delay of heating with depth. To relate phase to mixing rate, we modeled mixing as an effective diffusivity and numerically solved the heat equation for a system forced at the surface by a sinusoidal annual cycle for a range of diffusivities,  $\kappa_{eff}$ . A relationship was derived between  $\kappa_{eff}$  and the vertical gradient in phase of the resulting  $\mathcal{H}_{z_0}$ . Our results indicate an annual average of  $\kappa_{eff} \approx 10^{-3} \text{ m}^2 \text{ s}^{-1}$  over the upper 200 m of the water column in Drake Passage. While effective diffusivity may be an incomplete representation of a broad array of upper ocean mixing processes that are not strictly diffusive (e.g. entrainment), our value compares favorably to other measures of vertical diffusivities in this region (e.g.,  $O(10^{-3} \text{ m}^2 \text{ s}^{-1})$ ) [Thompson *et al.*, 2007].

## 5. Summary

[37] In this study, we have used XBT/XCTD profiles and reanalysis heat flux products to examine air-sea heat exchange in Drake Passage on a seasonal timescale. We

compared mixed-layer depth and heat content as two methods for measuring the response of the upper ocean to surface heat forcing. Results of this study show that upper ocean heat content is a robust indicator of upper ocean variability due to surface heat flux forcing in Drake Passage.

[38] Regional differences and temporal variability in Drake Passage stratification make it difficult to define MLD such that it is a true measure of the vertical extent of air-sea forcing. Estimates of  $MLD_T$  and  $MLD_\rho$  can disagree, suggesting that temperature alone is inadequate to unambiguously determine MLD. Further, as a result of low wintertime stratification, MLD estimates are not always robust; low-amplitude forcing or slight changes to the criteria used to define MLD can lead to large changes in MLD estimates. Perhaps as a consequence of the sensitivity of MLD calculations to small differences in temperature profiles,  $MLD_T$  also shows considerable variability at small horizontal scales.

[39] In contrast to MLD, upper ocean heat content is a robust measure of upper ocean variability. Average cast-to-cast differences in  $\mathcal{H}_{400}$  were 3 to 10 times smaller than in  $\mathcal{H}_{ML}$ ; the cast-to-cast variability in  $\mathcal{H}_{400}$  also changed less with season and less between the zones north and south of the Polar Front than cast-to-cast variability in  $\mathcal{H}_{ML}$ . This suggests that  $\mathcal{H}_{400}$  is a consistent measure of upper ocean variability north and south of the Polar Front and in both winter and summer.

[40] A first-order heat balance between the seasonal cycles of anomalous heat fluxes (minus the annual mean) and upper ocean heat content explains a large fraction ( $\sim 60\%$ ) of the variance of upper ocean heat content to 400 m depth south of the Polar Front and to a lesser extent ( $\sim 24\%$ ) north of the Polar Front. In contrast, an annual cycle that used heat content over the mixed layer did not match the surface-flux driven annual cycle as well in phase or in amplitude. However, the phase and amplitude of the seasonal cycle in  $\overline{\mathcal{H}}_{z_0}$  are somewhat sensitive to the choice of integration depth,  $z_0$ , particularly north of the Polar Front, where the amplitude increases and the date of the maximum heat content is delayed as integration depth increases. This is a result of heat mixing more deeply north of the Polar Front than south.

[41] Although we found reasonable agreement between seasonal cycles in upper ocean heat content and heat fluxes, the simple 1-D heat budget employed in this study may not be a complete picture of the processes governing upper ocean variability. Horizontal advection, whether zonal advection by the mean ACC flow or meridional Ekman transport, is likely to be an important component of a full upper ocean heat budget. Particularly north of the Polar Front, advection of eddies through Drake Passage may represent a large but transient departure from the seasonal cycles of upper ocean heat content we have calculated here. These processes will be important to consider in constructing a more complete understanding of the upper ocean response to air-sea fluxes.

[42] We have shown that upper ocean heat content can be a useful measure of the effects of air-sea heat flux forcing and may be more suitable for this purpose than MLD. One of the attractions of using MLD in studies of the Southern Ocean is the ability to couple remote-sensing observations of SST to an upper ocean heat budget. As in situ data in the Southern Ocean become more widely available, the need for

this proxy measurement of MLD that remotely sensed SST provides may be reduced. With the advent of Argo profiling floats, for example, there are now a few thousand profiles collected each year in the Southern Ocean, offering the prospect to observe the impact of upper ocean heating and cooling directly.

[43] **Acknowledgments.** Data collection and analysis for this project were funded by NSF grants to S.T.G. (ARRA OCE08050350) and J.S. (ANT0943818) and a NASA grant to S.T.G. (NNX08A182G). G.R.S. would like to acknowledge a NASA Earth and Space Science Fellowship and the ARCS Foundation for their support. S.T.G. acknowledges sabbatical support from the French Centre National de la Recherche Scientifique.

## References

- Bindoff, N. L., and T. J. McDougall (2000), Decadal changes along an Indian Ocean section at 32°S and their interpretation, *J. Phys. Oceanogr.*, *30*, 1207–1222.
- Boé, J., A. Hall, and X. Qu (2009), Deep ocean heat uptake as a major source of spread in transient climate change simulations, *Geophys. Res. Lett.*, *36*, L22701, doi:10.1029/2009GL040845.
- Böning, C. W., A. Disper, M. Visbeck, S. R. Rintoul, and F. U. Schwarzkopf (2008), The response of the Antarctic Circumpolar Current to recent climate change, *Nat. Geosci.*, *1*, 864–869.
- Brainerd, K. E., and M. C. Gregg (1995), Surface mixed and mixing layers, *Deep Sea Res.*, *9*, 1521–1543.
- Church, J., J. Gregory, N. White, S. Platten, and J. Mitrovica (2011), Understanding and projecting sea level change, *Oceanography*, *24*, 130–143.
- de Boyer Montégut, C., G. Madec, A. S. Fischer, A. Lazar, and D. Iudicone (2004), Mixed layer depth over the global ocean: An examination of profile data and a profile-based climatology, *J. Geophys. Res.*, *109*, C12003, doi:10.1029/2004JC002378.
- Dong, S., S. T. Gille, and J. Sprintall (2007), An assessment of the Southern Ocean mixed layer heat budget, *J. Clim.*, *20*, 4425–4442.
- Dong, S., J. Sprintall, S. T. Gille, and L. Talley (2008), Southern Ocean mixed-layer depth from Argo float profiles, *J. Geophys. Res.*, *113*, C06013, doi:10.1029/2006JC004051.
- Durack, P. J., and S. E. Wijffels (2010), Fifty-year trends in global ocean salinities and their relationship to broad-scale warming, *J. Clim.*, *23*, 4342–4362.
- Gille, S. T. (2008), Decadal-scale temperature trends in the Southern Hemisphere ocean, *J. Clim.*, *21*(18), 4749–4765.
- Gille, S. T., A. Lombrozo, J. Sprintall, G. Stephenson, and R. Scarlet (2009), Anomalous spiking in spectra of XCTD temperature profiles, *J. Atmos. Oceanic Technol.*, *26*, 1157–1164.
- Hanawa, K., and L. D. Talley (2001), Mode waters, in *Ocean Circulation and Climate: Observing and Modelling the Global Ocean*, *Int. Geophys. Ser.*, vol. 77, edited by G. Seidler, J. Church, and J. Gould, chap. 5.4, pp. 373–386, Academic, San Diego, Calif.
- Hanawa, K., P. Rual, R. Bailey, A. Sy, and M. Szabados (1995), A new depth-time equation for Sippican or TSK T-7, T-6 and T-4 expendable bathythermographs (XBT), *Deep Sea Res., Part I*, *42*, 1423–1451.
- Holte, J., and L. Talley (2009), A new method for finding mixed layer depths with applications to Subantarctic Mode Water and Argo, *J. Atmos. Oceanic Technol.*, *26*, 1920–1939.
- Jiang, C., S. Gille, J. Sprintall, K. Yoshimura, and M. Kanamitsu (2012), Spatial variation in turbulent heat fluxes in Drake Passage, *J. Clim.*, *25*, 1470–1488.
- Joyce, T. M., S. L. Paterson, and R. C. Millard (1981), Anatomy of a cyclonic ring in the Drake Passage, *Deep Sea Res., Part A*, *28*, 1265–1287.
- Kara, A. B., P. A. Rochford, and H. E. Hurlburt (2003), Mixed layer depth variability over the global ocean, *J. Geophys. Res.*, *108*(C3), 3079, doi:10.1029/2000JC000736.
- Kubota, M., N. Iwasaka, S. Kizu, M. Konda, and K. Kutsuwada (2002), Japanese ocean flux datasets with use of remote sensing observations (J-OFURO), *J. Oceanogr.*, *58*, 213–225.
- Kuhnel, I., and B. Henderson-Sellers (1991), Mixed layer modeling with respect to ocean–atmosphere interactions in the eastern Indian Ocean, *Meteorol. Atmos. Phys.*, *46*(1–2), 51–64.
- Levitus, S., J. I. Antonov, T. P. Boyer, R. A. Locarnini, H. E. Garcia, and A. V. Mishonov (2009), Global ocean heat content 1955–2008 in light of recently revealed instrumentation problems, *Geophys. Res. Lett.*, *36*, L07608, doi:10.1029/2008GL037155.
- Orsi, A. H., T. Whitworth III, and W. D. Nowlin Jr. (1995), On the meridional extent and fronts of the Antarctic Circumpolar Current, *Deep Sea Res.*, *42*, 641–673.
- Price, J. F., R. A. Weller, and R. Pinkel (1986), Diurnal cycling: Observations and models of the upper ocean response to diurnal heating, cooling, and wind mixing, *J. Geophys. Res.*, *91*, 8411–8427.
- Qiu, B., and K. A. Kelly (1993), Upper-ocean heat balance in the Kuroshio Extension region, *J. Phys. Oceanogr.*, *23*, 2027–2041.
- Sokolov, S., and S. R. Rintoul (2009), Circumpolar structure and distribution of the Antarctic Circumpolar Current fronts: 2. Variability and relationship to sea surface height, *J. Geophys. Res.*, *104*, C11019, doi:10.1029/2008JC005248.
- Sprintall, J. (2003), Seasonal to interannual upper ocean variability in the Drake Passage, *J. Mar. Res.*, *61*, 27–57.
- Thompson, A. F., S. T. Gille, J. A. MacKinnon, and J. Sprintall (2007), Spatial and temporal patterns of small-scale mixing in Drake Passage, *J. Phys. Oceanogr.*, *37*, 572–592.
- Trenberth, K. E., and J. T. Fasullo (2010), Simulation of present day and 21st century energy budgets of the Southern Ocean, *J. Clim.*, *23*, 440–454.
- Yu, L., and R. Weller (2007), Objectively analyzed air-sea heat fluxes for the global ice-free oceans (1981–2005), *Bull. Am. Meteorol. Soc.*, *88*, 527–539.

S. T. Gille, J. Sprintall, and G. R. Stephenson Jr., Scripps Institution of Oceanography, University of California, San Diego, 9500 Gilman Dr., Mail Code 0230, La Jolla, CA 92093-0230, USA. (sgille@ucsd.edu; jsprintall@ucsd.edu; grstephe@ucsd.edu)